PHYSICAL REVIEW SPECIAL TOPICS - ACCELERATORS AND BEAMS **10**, 080101 (2007)

Superconducting CH structure

H. Podlech, U. Ratzinger, H. Klein, C. Commenda, H. Liebermann, and A. Sauer[*]

Institute for Applied Physics (IAP), University of Frankfurt, 60438 Frankfurt, Germany

(Received 27 March 2007; published 7 August 2007)

The superconducting CH structure is a novel multicell cavity for the acceleration of protons and ions in the low and intermediate energy regime. The CH structure is a cross-bar-type cavity; it is the first superconducting low energy multicell cavity operated in an H mode. A superconducting CH-prototype cavity with 19 gaps at $\beta = 0.1$ has been built and tested successfully. Maximum surface fields of 25 MV/m and a corresponding effective cavity voltage gain of 3.7 MV have been achieved. In this paper the development and the tests of this new cavity are presented. This includes also tuning and coupling methods as well as a comparison with other low energy cavities.

DOI: 10.1103/PhysRevSTAB.10.080101 PACS numbers: 29.17.+w, 85.25.Am, 52.70.Gw

I. INTRODUCTION

During the past 35 years some different types of short superconducting low and medium energy cavities $\beta = v/c < 0.5$ have been developed for ion and proton acceleration at nuclear research laboratories. Recently, there was an additional boost in this development mainly triggered by several new projects like RIA [1], SPIRAL-2 [2], and by facilities for applied research facilities like EUROTRANS [3], IFMIF [4], or TRASCO [5]. Single spoke and half-wave cavities have been pushed to very high gradients [3,6–12]. A common feature of all these cavities which had been developed so far is the limited number of accelerating cells. Depending on the cavity type, this number is between one and four: (i) *1 cell*—reentrant cavities; (ii) *2 cells*—quarter-wave and half-wave cavities, single spoke cavities; (iii) *3 cells*—double spoke cavities, split ring structures; (iv)*4 cells*—triple spoke cavities, interdigital quarter-wave cavities.

In many cases the rf linac efficiency can be increased significantly by the use of multicell cavities. For instance, in case of actual projects involving proton driver linacs with rf frequencies around 350 MHz there is an obvious lack of efficient superconducting low-β cavities. In these cases "efficient" means a high energy gain per cavity which leads to a low total number of individual cavities and rf systems. Because of the rf frequency and to the radio frequency quadrupole (RFQ) voltage gain which is typically between 1 and 5 MV, the cell length $\beta\lambda/2$ is around 40 mm at the superconducting drift tube linac (DTL) front end. Using conventional 2-gap structures (quarter-wave and half-wave cavities) reduces the filling factor significantly as cavities with a small number of cells imply a lot of drift spaces and increase the mechanical complexity of the linac significantly. The task to develop efficient superconducting DTL front ends with large filling factors and with high real estate gradients has motivated the design, construction, and test of the superconducting CH-type structure (see Fig. 1).

II. H-MODE CAVITIES

The CH structure belongs to the family of H-mode cavities which are operated in an H_{n1}-mode. This new structure has been named CH structure because of its cross-bar geometry and the H_{21} mode [13–15]. H-mode cavities have been developed and operated very successfully during the past 30 years [13,16–20]. Considering the two lowest modes (H_{11} and H_{21}), there are four types of accelerating cavities: (i) IH-DTL, H_{110} mode; (ii) IH-RFQ, H_{110} mode; (iii) 4-vane-RFQ, H_{210} mode; (iv) CH-DTL, H_{210} mode.

Figure 2 shows an IH-DTL, a room temperature (rt) CH-DTL, and a superconducting (sc) CH-DTL. In many inter-

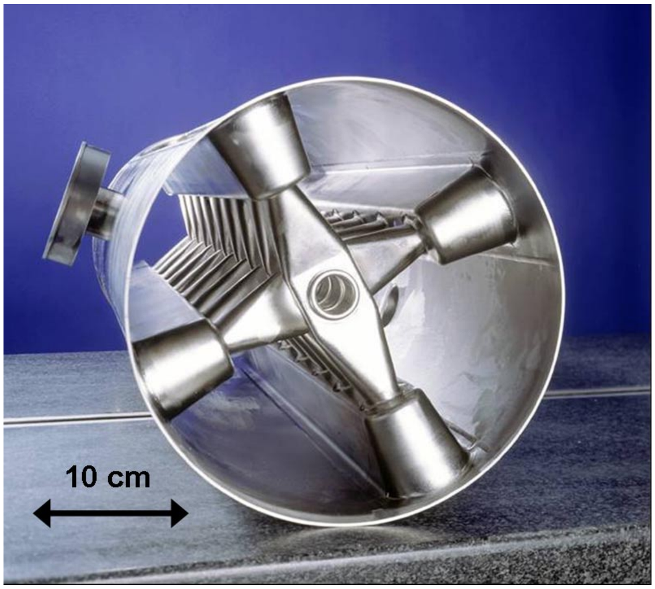

FIG. 1. (Color) View into the superconducting CH cavity, $\beta = 0.1$, $f = 360$ MHz, before welding of the end walls (courtesy ACCEL, Bergisch-Gladbach, Germany).

---

[*] h.podlech@iap.uni-frankfurt.de; http://linac-world.de

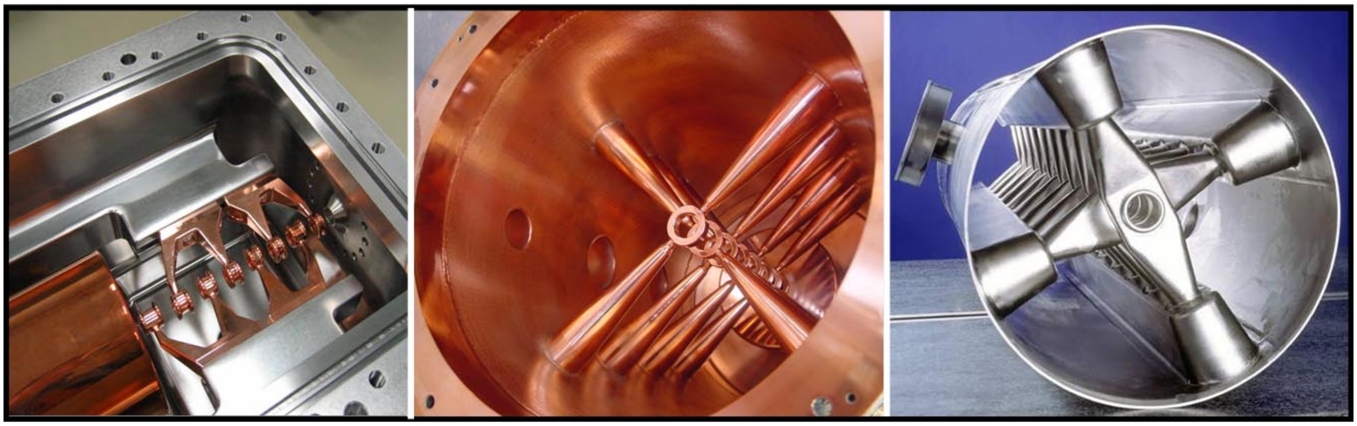

FIG. 2. (Color) H-mode drift-tube cavities: rt IH-DTL (217 MHz, left), rt CH-DTL (350 MHz, center) and sc CH-DTL (350 MHz, right).

digital H-mode (IH) structures the drift tubes are mounted on girders with undercuts at the end (Fig. 2, left). The undercuts increase the magnetic flux close to the end flanges which helps to obtain a flat field distribution. In CH structures no undercuts are needed. The field distribution is achieved by using longer half drift tubes and by adequate end-cell geometry. In general, H-mode structures have high acceleration efficiencies at the low and medium energy range. The rt IH-DTL has no competitor with respect to efficiency and shunt impedance in the low energy range from $\beta = 0.01$–0.2. For β values up to 0.1, the plug power needed to operate an IH linac is competitive with superconducting solutions at identical accelerator length. Figure 3 shows the effective shunt impedance $Z_{\mathrm{eff}} = Z_0 T^2 \cos^2\phi$ (Φ = synchronous phase) as a function of the particle velocity $\beta = v/c$ [13,21,22]. Very high gradients of up to 10.7 MV/m in pulsed operation have been achieved in IH structures [23] and cw operation has been demonstrated from the very beginning [24,25]. However, the IH-type cavity does not seem to be suited for sc linac development because of a lack of mechanical stability as required for superconducting cavities. Additionally, due to its small transverse dimensions the maximum reasonable IH-DTL frequency is about 250 MHz which is too low in many cases. The CH structure with its crossed stem geometry provides the needed mechanical rigidity. Moreover, in the H_{21} mode the operation frequency can be up to 800 MHz [13,15]. CH-cavity diameters are very convenient for fabrication up to that rf frequency. One main feature of IH and CH structures which boosts the efficiency and makes long multicell cavities possible is the KONUS (Kombinierte-Null-Grad-Struktur) beam dynamics [13,14,26]. The KONUS concept reduces the transverse rf defocusing by using 0° main accelerating sections. A KONUS-period consists of three sections with separate functions. The first section consists of a few gaps with a negative synchronous phase of typically $-30°$ to $-35°$ and acts as a rebuncher. The beam is then injected into the 0° section with a surplus in energy compared with a "synchronous" particle. This multigap main accelerating section is then followed by transverse focusing elements which are magnetic quadrupole triplets. IH cavities with up to 56 gaps and with three internal triplets have been realized [21,27]. Superconducting CH cavities will house only the rebuncher and the main acceleration section. The transverse focusing elements will be located in the intertank sections. The number of cells in each section depends mainly on the rf frequency, on the gradient, and on the beam current. It was shown that high beam currents can be accelerated in H-mode structures with KONUS beam dynamics [18,26]. Depending on frequency, on beam velocity, and on beam current, between 5 and 30 gaps per section can be realized for different applications. Because of the large number of accelerating cells resulting in a large energy gain the change in beam velocity can be significant. Therefore all multicell H-mode

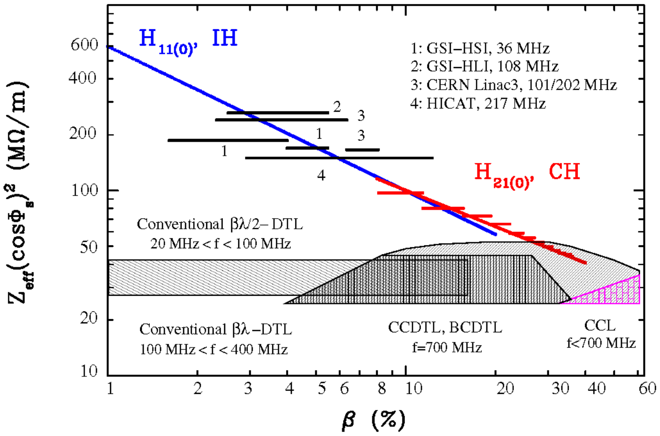

FIG. 3. (Color) Effective shunt impedance for different rf structures including the transit time factor T and the synchronous phase ϕ as a function of the particle velocity $\beta = v/c$. The black horizontal bars represent some existing IH-DTLs [13,21,22] and the red bars represent the expected shunt impedance of the rt CH cavities for the GSI-FAIR 70 MeV, 70 mA proton linac [57].

drift-tube structures have a graded β-profile. As a consequence, the bunch phases in all gaps are kept at an optimum as well as the transit time factor. On the other hand, multigap cavities with a fixed β-profile have effective acceleration voltages $U_{a,i} = U_{0,i} T_i \cos\varphi_i$ depending on the beam energy for each gap. When shorter cavities with a fixed β are applied for a wider energy range, they provide an optimum transit time factor only for one specific particle velocity.

III. FIELD DISTRIBUTION IN GENERAL

The magnetic field of the H_{211} mode used in the CH structure penetrates among the four quadrants. The voltage U_i in the ith gap can be calculated from the induction law:

$$U_i = -\dot{\Phi} = -\int_{\mathrm{quad}} \dot{B}_z dA. \tag{1}$$

B_z is the rather homogeneously distributed B_z field across each quadrant. The integration has to be done over one quadrant. Without end cells, the resulting sinoidal dependence of the longitudinal magnetic field in the z direction leads directly to a sinoidal electric gap field and voltage distribution, respectively. To reduce the electric and magnetic peak field and to fulfil the beam dynamics requirements, it is necessary to obtain a flat electric gap field distribution along the cavity. An important detail of a CH structure is the end-cell geometry. Figure 4 shows a cut through the CH cavity with the definition of the end cell. In this area the longitudinal magnetic flux is bent by 180 degrees from one quadrant into the neighboring quadrants. A lower end-cell resonance frequency causes a local field increase. In the case of room temperature H-mode structures (4-vane-RFQ, IH-DTL), the inductance at the cavity end is increased by using undercuts in the vanes or in the girders, respectively. But in the case of superconducting CH structures this leads to unacceptably high magnetic fields in this area [28]. On the other hand, the fabrication of the cavity should be as easy as possible. Therefore different end-cell geometries have been investigated [29].

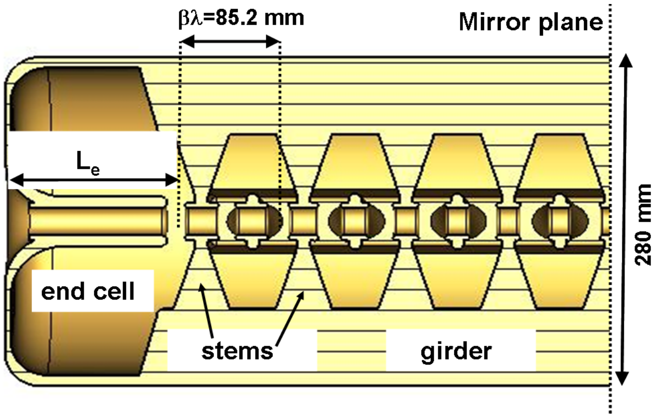

FIG. 4. (Color) 2D cut of the realized sc CH-cavity geometry.

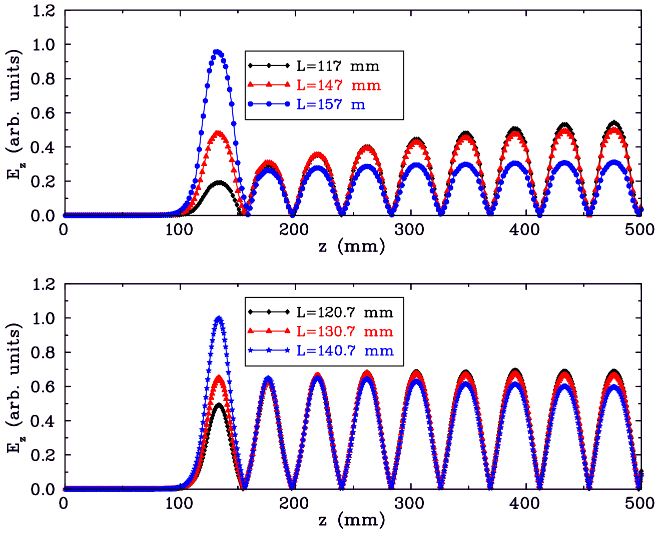

FIG. 5. (Color) Top: Simulated electric gap field distribution for different end-cell lengths and constant g/L ratio of 0.5. Bottom: Simulated electric gap field distribution for different end-cell lengths and variable g/L ratios.

In general, it is possible to change the tank radius in the end-cell region or to change the length of the end cell. From the production point of view, it was easier to change the length. Figure 5 shows the simulated electric gap field distribution for different end-cell lengths L_e. The upper plot represents the prototype geometry with constant gap-to-cell length ratio $g/L = 0.5$ and the lower plot represents the geometry with variable g/L ratio which leads to a flat electric field distribution. The end-cell length has a major impact on the field distribution and on the field strength in the first and the last gap.

IV. GIRDER SIZE

One important geometrical feature of the superconducting CH structure is the girders. The girders partly separate

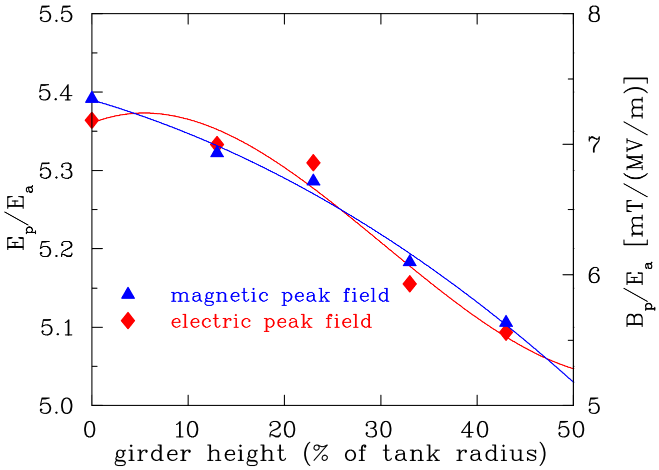

FIG. 6. (Color) Simulated influence of the girder height on the electric and magnetic peak fields.

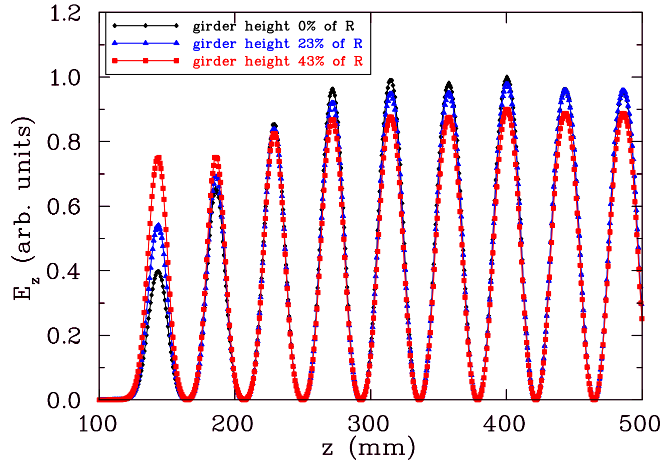

FIG. 7. (Color) Simulated electric gap field distribution for three different girder heights (0%, 23%, and 43% at a constant tank radius $R = 140$ mm). The girder height of $0.43R$ corresponds to the prototype geometry. Because of the cavity symmetry only one-half of the length is shown. Each gap voltage corresponds to the local magnetic flux [see Eq. (1)].

the CH cavity into four chambers which are penetrated by the longitudinal magnetic flux of the H_{21} mode. The girders can be considered as a broad common extension of the stems. Similar to half-wave resonators, the maximum current density typically occurs at the stem base. The girders broaden the current path and reduce the current density. Therefore it was expected that the use of girders reduces the magnetic peak field. Figure 6 shows the influence of the girder height on the magnetic and electric peak fields. This simulation shows the expected decrease in the magnetic peak field with higher girders. Additionally, a decrease in the electric peak field can be recognized because the girders improve the electric field flatness as can be seen in Fig. 7. The girders lead to a very homogeneous current distribution which reduces the magnetic peak field. Figure 8 shows the longitudinal magnetic field distribution. The data have been taken at three different positions across the cavity for different girder heights h (Fig. 8, part 4). In all cases the H mode is well established. The disadvantage of girders without walls at the outer cavity radius is a lower mechanical stability against external pressure. To provide

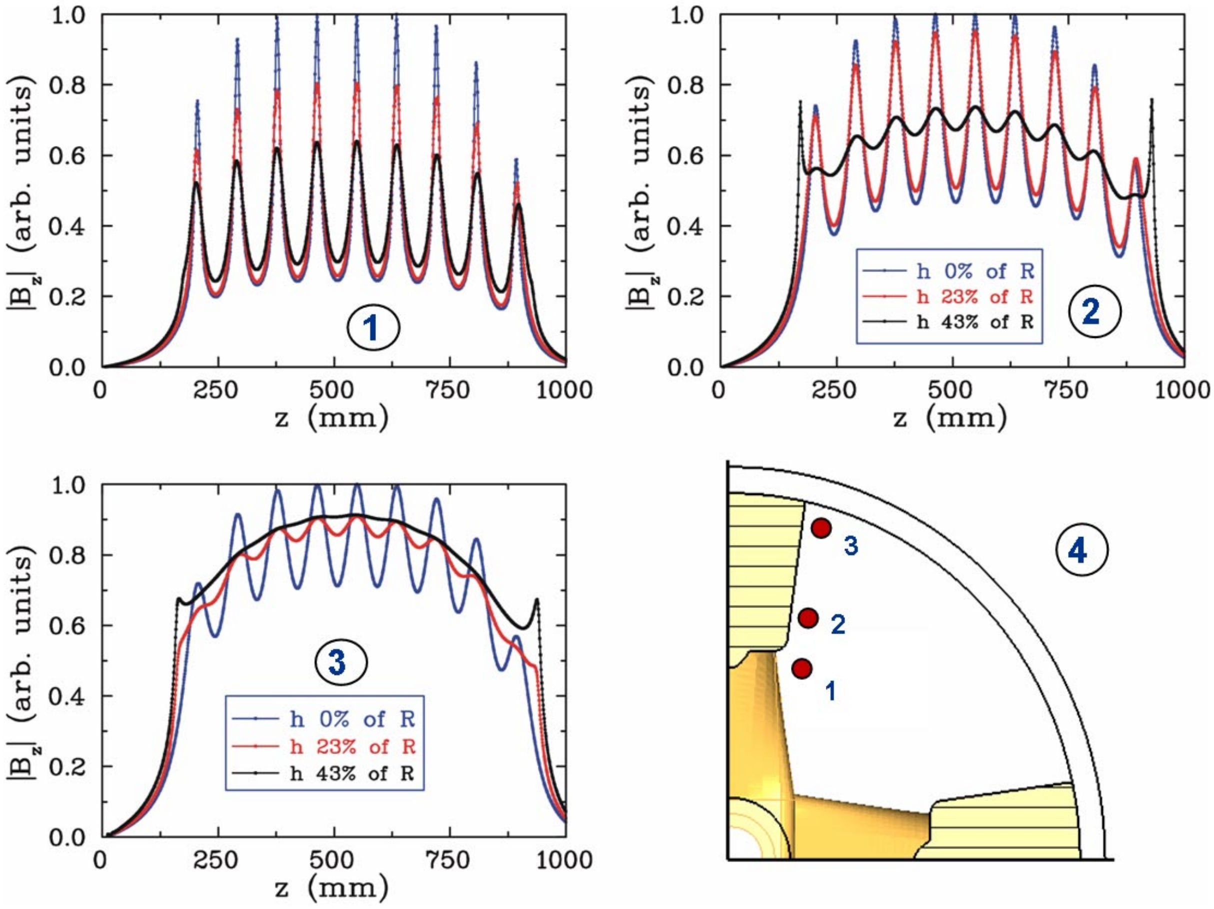

FIG. 8. (Color) Plot of the magnetic field $|B_z|$ along the CH cavity. The field is shown for three different paths along the cavity. The girders support a flat field distribution along a CH cavity and lead to very homogeneous local current densities which reduce the magnetic peak fields.

enough stability several rings had to be welded around the cavity. But girders provide quite a number of advantages when used in superconducting CH cavities. They improve the capacitive coupling for the power coupler mounted in transverse direction into the girder between stems (Fig. 14). The inner conductor of the coaxial standard feeder is facing a drift tube excited in opposite polarity. A relatively strong coupling is required for high current applications. Therefore it is important to place the coupler in a position close enough to a drift tube. Additionally, the girders shield the coupler from the magnetic fields which might cause additional losses otherwise. The girders provide also a nice capacitive tuning concept to be applied during the cavity fabrication as described below.

V. PEAK FIELD OPTIMIZATION

A study has been performed to investigate the dependence of the electric and magnetic peak fields from different geometrical parameters. Figure 9 shows the electric field along a path perpendicular to the beam axis in case of different drift-tube thicknesses ΔR. The peak field at the tube ends is only slightly decreasing for thicker drift tubes above the prototype parameter $\Delta R = 5$ mm. On the other hand, the most efficient way for peak surface field reduction is a choice of the g/L ratio as large as possible with respect to acceleration field aberrations as well as to mechanical stability in each case. The magnetic peak field can be optimized by varying the stem geometry. Figure 10 shows the magnetic and electric peak fields as a function of the stem width b. While the electric peak field is nearly independent of the stem width the magnetic peak field decreases with larger stem width. For a given half axis a, the magnetic peak field reaches the flat plateau for $a \approx b$. Table I summarizes the important parameters of the CH-prototype cavity. The electromagnetic design of the CH-prototype cavity has been performed using MICROWAVESTUDIO (MWS) [30].

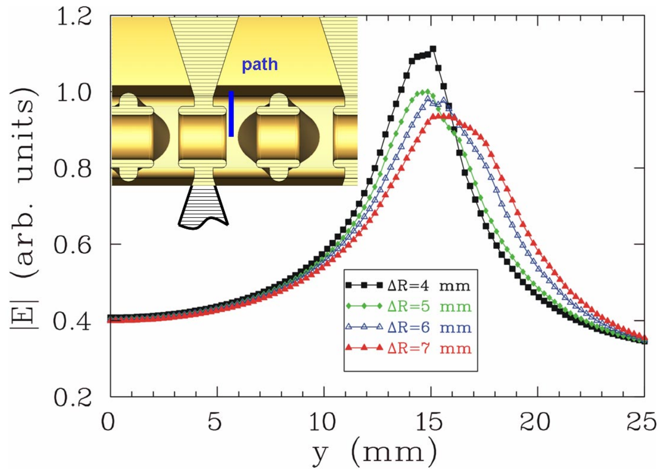

FIG. 9. (Color) Electric field along a path perpendicular to the beam axis for different drift-tube wall thicknesses ΔR. The field is normalized to the maximum field for $\Delta R = 5$ mm (prototype geometry). The path distance from the tube ends is 2 mm in all cases. The aperture diameter is 25 mm in all cases, the g/L ratio is 0.5, $L = 42.6$ mm.

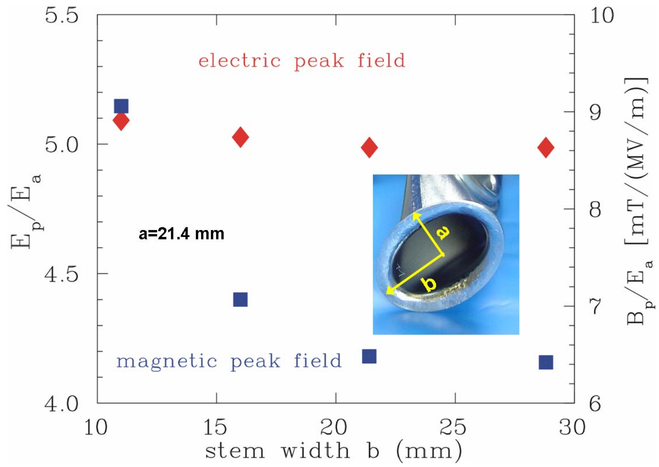

FIG. 10. (Color) Electric and magnetic peak field as a function of the stem width b at constant a and $L = 42.6$ mm. The peak fields are based on the $\beta\lambda$ definition of the gradient.

TABLE I. Parameters of the superconducting CH prototype cavity.

Cavity type	Cross-bar H mode
β	0.1
Frequency (MHz)	360
Accelerating cells	19
Material	Bulk niobium
RRR	250
Length (mm)	1048
Diameter (mm)	274
G (Ω)	56
Q_0 (BCS)	1.3×10^9
R_a/Q_0 (Ω)	3180
R_a/Q_0 per cell (Ω)	167
GR_a/Q_0 (kΩ^2)	178
E_p/E_a $\beta\lambda$-definition	5.2
B_p/E_a $\beta\lambda$-definition [mT/(MV/m)]	5.7
E_p/E_a total length	6.6
B_p/E_a total length [mT/(MV/m)]	7.3
W/E_a [mJ/(MV/m)^2]	92 ($\beta\lambda$-definition)

VI. FIELD TUNING

A room temperature copper model has been built to validate the results obtained by MICROWAVESTUDIO [28]. Figure 11 shows the copper model. The number of cells, the cell length, and the gap-to-cell-length ratio g/L can be varied. The copper model has been used to demonstrate different tuning and coupling methods in CH structures.

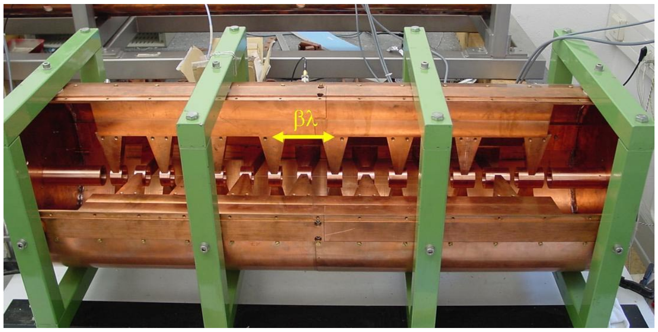

FIG. 11. (Color) The room temperature copper model which has been used to validate the electromagnetic simulations. This photograph shows the model with a graded beta from 0.085 to 0.12.

Depending on the cell length, the model has between 9 and 20 gaps. The particle β can be varied between 0.07 and 0.2. A major concern was the minimization of electric and magnetic peak fields. To minimize these fields and to fulfill the requirements of the beam dynamics, it is necessary to approach a flat gap field distribution. The field distribution of an H-mode cavity with constant capacitive load per unit length and without resonant end cells is sinoidal. The "0 mode" is established by changing the gap-to-drift-tube-length ratio per cell and by using resonant end cells. Figure 12 shows the optimized field distribution with β-profile (measured and simulated) and Fig. 13 shows the tube and gap lengths which are required to achieve the flat field distribution. It has been demonstrated that a sufficiently flat distribution can be achieved in CH structures with β-profile [31]. The maximum deviation between the simulated and measured gap voltage is less than the required value of 5%.

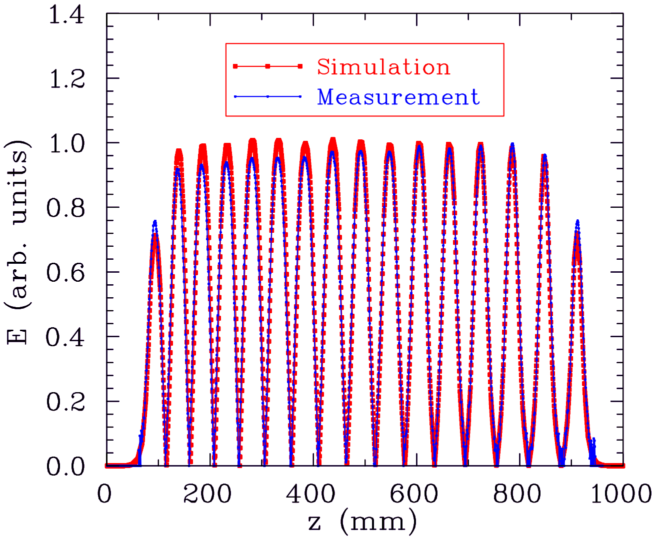

FIG. 12. (Color) Comparison between the measured and the simulated field distribution of the CH-copper model as shown in Fig. 11.

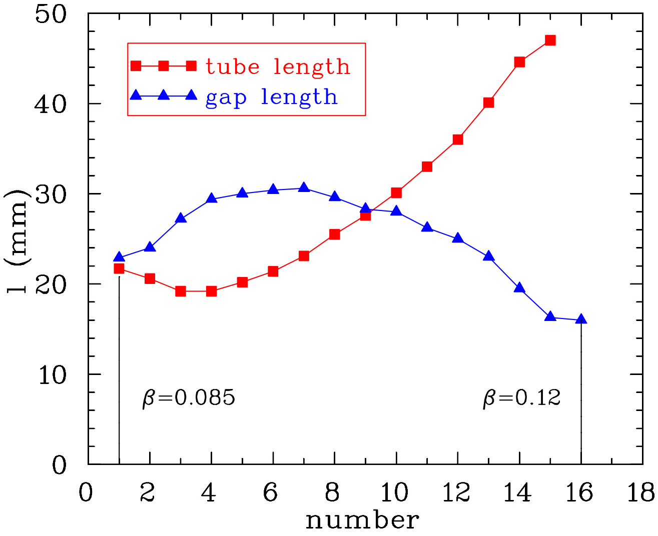

FIG. 13. (Color) Gap and drift-tube lengths which are required to obtain the flat field distribution in Fig. 12.

VII. RF COUPLING

The rf coupler must provide enough coupling strength to be critically coupled at maximum beam load. Depending on the application an external Q-value between 10^7 and 10^4 must be reached for the superconducting CH structure. Usually in superconducting cavities the rf power is coupled via capacitive couplers. Besides this type of coupling, we also investigated inductive coupling which is used in nearly all operated room temperature cavities. It has been shown that both methods could be used to reach the required coupling for superconducting CH structures. But, of course, in practice capacitively acting power couplers will be used which have been developed successfully at several laboratories already [32–34]

A. Capacitive power coupler

The best position to place the capacitive coupler in case of superconducting CH structures is through the girder. At this position, the electric field is high enough to provide sufficient coupling and the magnetic field is low enough to avoid excessive heat production in the coupler. Figure 14 shows the position of the capacitive coupler which has been used in the room temperature copper model to determine the coupling strength theoretically and experimentally. The external Q-value which measures the coupling strength has been calculated numerically with a method proposed in [35]. For each data point two MWS simulations of a coupler with transmission line have been performed, one with electric and one with magnetic boundary conditions. The external Q-value is then described by

$$Q_e = \frac{2fW}{cr_0^2 \ln(b/a)}\left(\frac{1}{\epsilon_0|E_0|^2} + \frac{\mu_0}{|B_0|^2}\right). \tag{2}$$

r_0 is any position between inner and outer conductor with

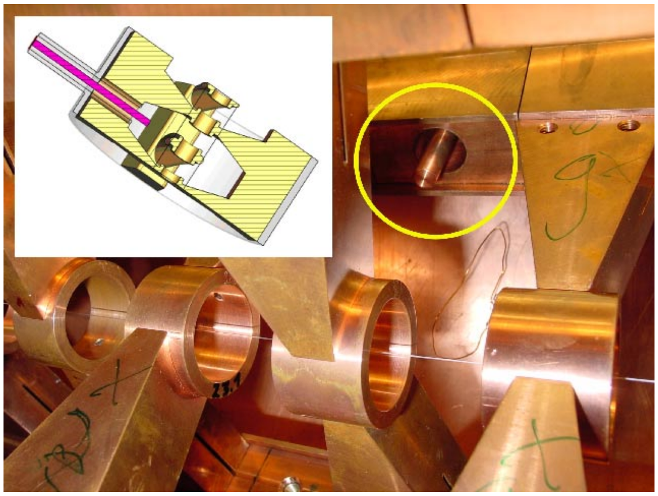

FIG. 14. (Color) The picture shows the favored location of the capacitive coupler during investigations with the room temperature copper model.

FIG. 16. (Color) The picture shows the location of the inductive coupler in the room temperature copper model. The external Q-value has been varied by changing the loop angle.

corresponding fields $E_{0,r}$ and $B_{0,r}$. Figure 15 shows the comparison of the external Q-value as a function of the coupler position between the theoretical model and the measurements. At high external Q values, the data points have been taken in transmission. The agreement between theoretical and experimental values is good over more than 6 orders of magnitude. With a coupler tip radius of 4 mm an external Q-value of less than 10^4 could be reached when diving the inner conductor 40 mm into the cavity. However, for high power cw applications a coupler with larger diameter will be used.

B. Inductive power coupler

Another possibility to couple rf power to a superconducting cavity is the inductive coupling via a coupling loop. Inductive coupling to a superconducting cavity has been used successfully for the first time at FZ Jülich, Germany [36]. Figure 16 shows the position of the loop in the room temperature model. The loop angle is set to 90° for the minimum external Q value. In this case the magnetic flux which is longitudinal and homogeneous is in good approximation perpendicular to the loop area. With the well justified assumption that the magnetic field is constant over the loop area, the external Q value can be calculated:

$$Q_e = \frac{W \cdot 50\ \Omega}{\omega(A_s \cdot B_0 \cdot \cos\alpha)^2}. \tag{3}$$

W is the stored energy and A_s is the loop area. The external Q value has been numerically calculated using the same method as for the capacitive coupling. Figure 17 shows the

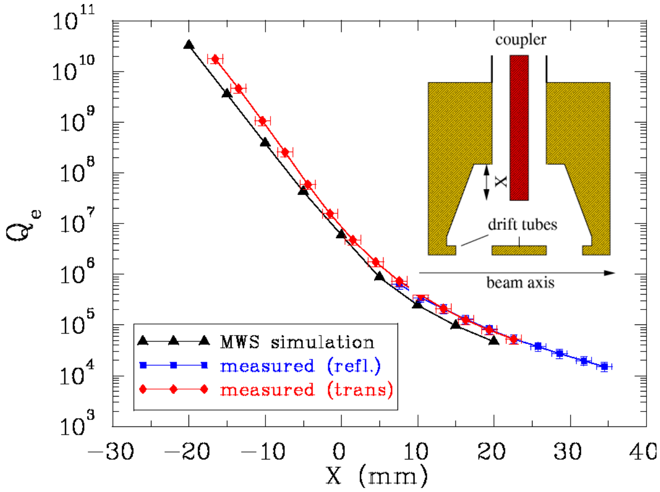

FIG. 15. (Color) Comparison between measurement and simulation of the external Q-value as a function of the position of the capacitive coupler.

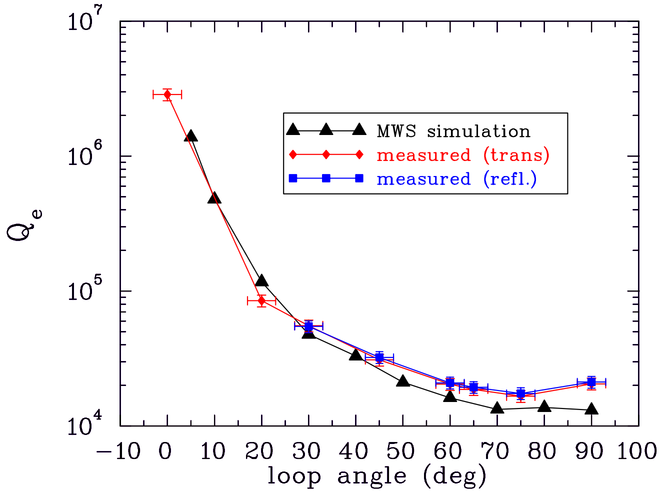

FIG. 17. (Color) Comparison between measurement and simulation of the external Q-value as a function of the loop angle.

comparison between simulation and measurement of Q_e as a function of the loop angle. A loop with an area of 2 cm × 3 cm has been used. For comparison, the diameter of the used cavity model is 300 mm. The $1/(\cos\alpha)^2$ dependence can be clearly recognized. With the used loop an external Q value between 1×10^4 and 3×10^6 could be reached. The Q value at $\alpha = 0$ is dominated by a capacitive loop coupling effect. As for the capacitive coupling the agreement between simulation and measurement is very good.

VIII. CAVITY FABRICATION

Prior to production, a study has been performed together with the company ACCEL, Germany [37] which showed the feasibility of realizing a complex cavity like the CH structure. The prototype cavity has then been fabricated by ACCEL. The cavity is made from bulk niobium sheets with a thickness of 2 mm and with a RRR value of 250. All parts have been formed either by deep drawing or by spinning. For the cavity production electron beam welding was applied. Figure 18 shows a part of the inner structure during the fabrication. One special feature of this prototype are the drift tubes which have been welded into the stems. The length of each drift tube is different to guarantee a constant field distribution. After the final welding, the cavity has been treated with temperature controlled buffered chemical polishing to remove about 120 μm from the surface followed by high pressure rinsing using a pressure of about 80 bar (performed by ACCEL).

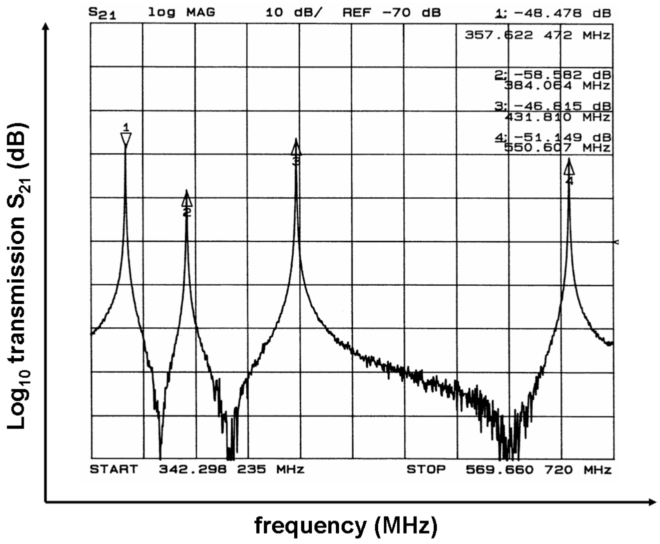

FIG. 19. The first low level rf measurement at room temperature shows the mode spectrum between 340 and 570 MHz. The ordinate scale is 10 dB/division, the frequency is swept between 342 and 570 MHz.

IX. RF MEASUREMENTS AND FIELD TUNING DURING THE PROTOTYPE PRODUCTION

During the fabrication of the cavity measurements at room temperature have been performed. Figure 19 shows the first measured mode spectrum between 340 and 570 MHz. The first peak with a frequency of 359 MHz is the H_{21} mode. Because of the strong magnetic coupling between the cells neighboring modes are well separated. A new method to tune the field distribution and the frequency in multicell CH cavities has been applied, which is especially suited for superconducting cavities. Adding cylindrical tuning blocks between the stems increases locally the capacitance. This influences the field distribution and the frequency. In the superconducting CH prototype 10 cylindrical tuners have been integrated. Before the final welding of the end cells, the frequency and the field distribution have been measured as a function of the tuner height. Brass tuners (plungers) with variable height have been used. Figure 20 shows one single tuner and the

FIG. 18. (Color) Drift-tube structure from bulk niobium welded into one pair of girders during fabrication (courtesy ACCEL).

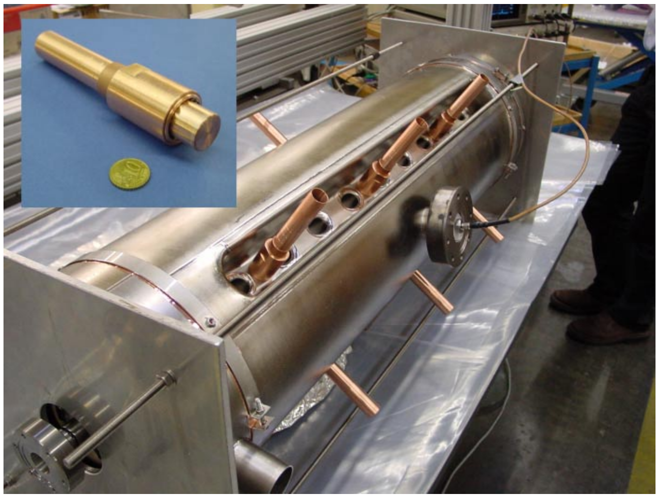

FIG. 20. (Color) Setup for the frequency and field tuning of the superconducting CH prototype. Ten movable tuners (top left) have been used to tune the cavity.

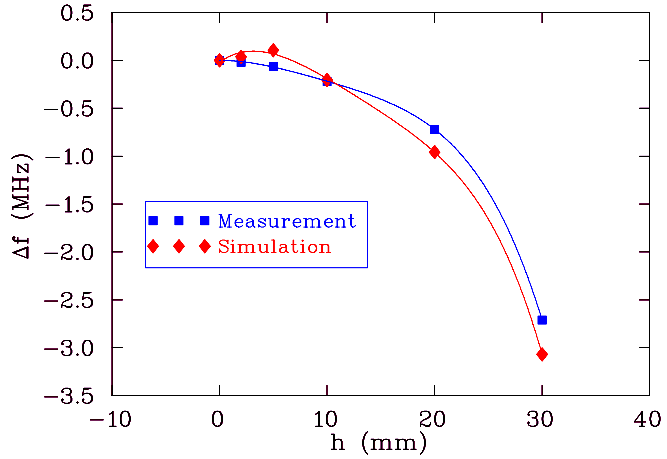

FIG. 21. (Color) Comparison between the measured and simulated frequency shift using the tuners shown in Fig. 20. With an identical tuner height of 30 mm for all 10 tuners a frequency shift of almost −1% of the resonance frequency could be achieved.

experimental setup with 10 tuners. The radius of each tuner is 10 mm. The rf contact was provided by spring contacts. By changing the different tuner heights it was possible to change the field distribution significantly and to shift the frequency by almost up to −1% of the initial resonance frequency. Figure 21 shows the simulated and measured frequency shifts as a function of an identical tuner height for all 10 tuners. The predicted shift of about −1% for tuner heights of 30 mm could be validated experimentally. The frequency is decreasing with a larger tuner height because of the higher capacitance per unit length. A positive frequency shift at small tuner heights was predicted by MWS simulations. But this has not been observed experimentally. It is assumed that the cell grid at the wall was not adequate to describe this effect correctly. Figure 22 shows the frequency shift as a function of the tuner radius R_T at a constant tuner height h.

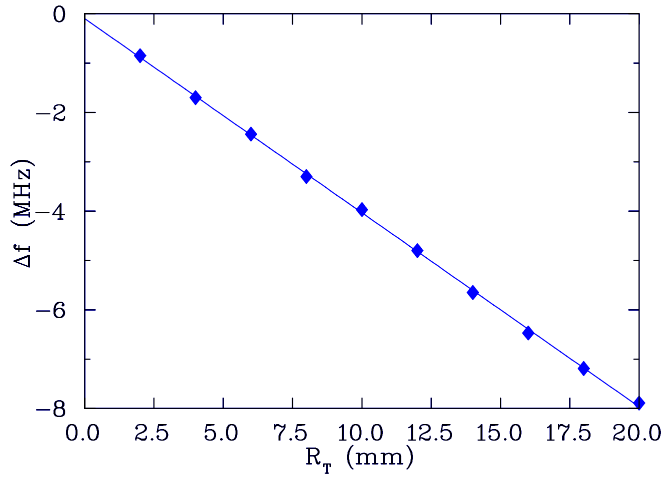

FIG. 22. (Color) Simulated frequency shift as a function of the tuner radius R_T at a constant tuner height of $h = 30$ mm.

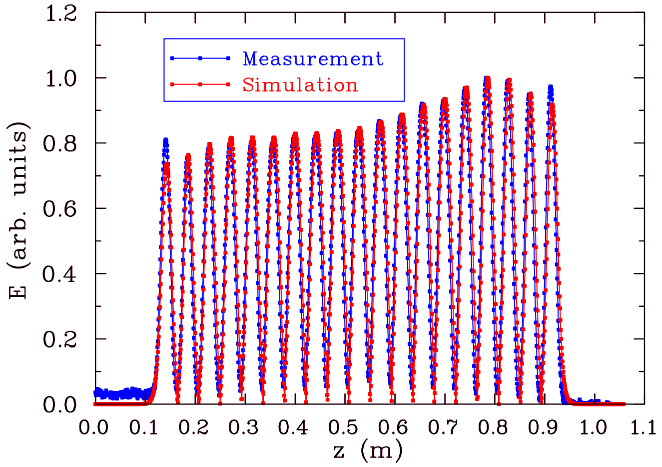

FIG. 23. (Color) Using different heights for the tuners, it was possible to change the field distribution in a well-defined way. Here only 3 tuners with a height of 30 mm have been installed at the right side.

By changing the capacitance locally via plungers it was possible to influence the gap field distribution in a well-defined way. In general, the gap fields increase in a region of higher capacitive load. With the use of three tuners ($h = 30$ mm) in the right side of the cavity the field could be tilted by about 20% (Fig. 23). Using 6 tuners ($h = 30$ mm) in the left and right side, a central dip of about 10% in the field distribution could be created (Fig. 24). Finally, the field distribution has been optimized by using different heights of the tuners (0, 10, and 20 mm) along the cavity. The obtained gap voltage distribution is within ±2.5% deviation to nominal gap voltages as defined by beam dynamics calculations. This agreement is sufficient in most linac design cases. Figure 25 shows the optimized field distribution of the CH prototype as measured before the final welding. Additionally, in Figs. 23–25 the field distributions obtained by simulations are shown. In all

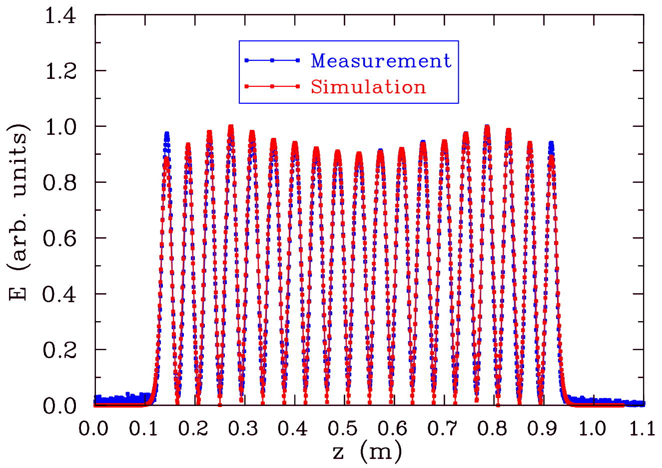

FIG. 24. (Color) This field distribution has been obtained by installing 3 tuners at each cavity end with a height of 30 mm.

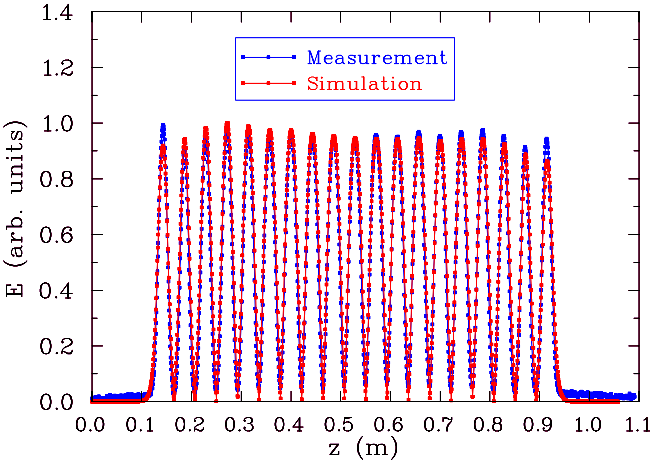

FIG. 25. (Color) Comparison between measurement and simulation of the final field distribution. Ten tuners with heights of 0, 10, and 20 mm have been used. The field flatness is very good and sufficient for most of the applications.

three cases the agreement is very good. After this tuning procedure, the plungers have been replaced by high RRR niobium tuner blocks which then have been welded into the girders. H-mode drift-tube cavities typically do not show much multipacting. The reason is that the electromagnetic fields close to the surface, especially in the vicinity of the stems, are very inhomogeneous. This makes it very unlikely to produce stable resonance conditions for multipacting. It has been decided to precondition the prototype cavity with rf power at room temperature. For this reason the cavity has been equipped with a critically coupled loop coupler. An rf power of up to 300 W cw has been coupled into the cavity. The temperature at four different positions has been measured. Figure 26 shows the position of the temperature sensors and the measured temperature of the cavity. As expected, the temperature reached the highest values close to the stem base where the current density has a maximum. Finally, up to 2 kW with 5% duty cycle (100 μs, 500 Hz) has been coupled in the cavity. At a power level just below 2 kW a multipacting barrier has been observed. This corresponds to a gap voltage U_a of 8 kV. The pressure after conditioning has improved from 6×10^{-8} hPa to 2×10^{-8} hPa.

X. COLD TEST OF THE PROTOTYPE CAVITY

To test the superconducting CH structure a cryogenic rf laboratory has been established in Frankfurt. It has been equipped with a 3 m high vertical cryostat, transport dewars, a class 10 000 clean room, a helium recovery system, a 2 kW cw amplifier, and the control system. Figure 27 shows the experimental setup for the first cryotest of the superconducting CH structure. Around the cryostat a magnetic shielding with a thickness of 2 mm has been placed. This shielding attenuates the magnetic field at the cavity to about 2 μT. To save helium the cavity has been precooled with liquid nitrogen. Figure 28 shows a schematic drawing of the function principle of the control system which has been developed in Frankfurt. At very low power levels ($P_f \approx$ mW) several multipacting barriers have been observed. It turned out that the most efficient way to process these barriers was to sweep over the resonance with a forward power of about 10 W. After 2–3 hours the first barrier has been conditioned. The conditioning of higher barriers took much shorter time in the order of minutes. Figure 29 shows a typical multipacting case observed with a network analyzer measuring the tank signal. Figure 30 shows the rf signals of the superconducting CH structure at a high field level corresponding to critical coupling ($U_a \approx$ 3 MV). At low field levels, the decay time for the stored energy τ_L was 50 ms. Together with the frequency of 360 MHz, this resulted in a loaded Q value of 1.13×10^8. The input coupler was overcoupled at low field levels. This was intended because stronger coupling typically

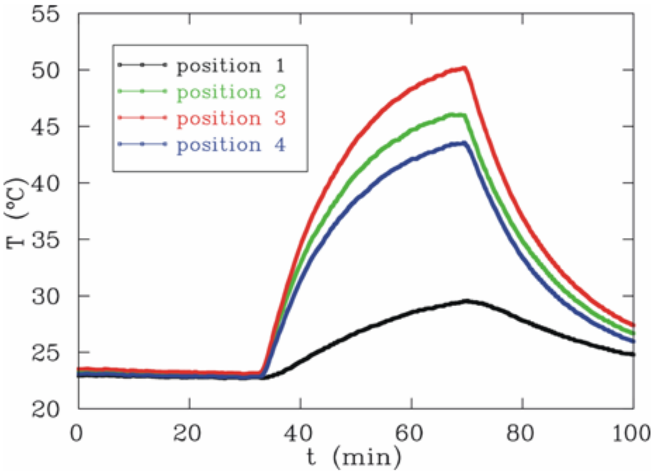

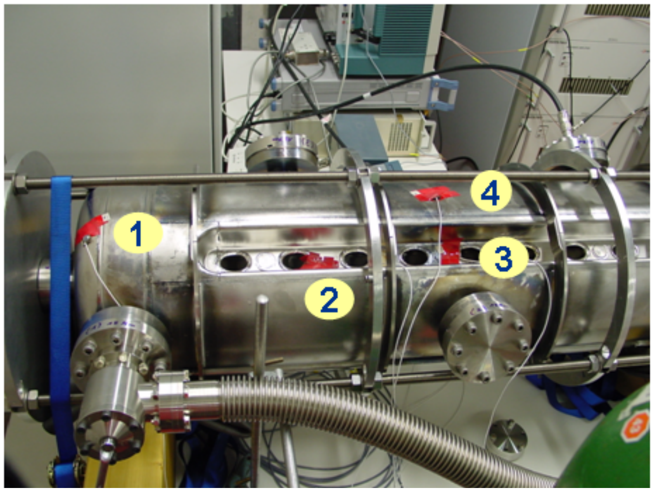

FIG. 26. (Color) Several temperature sensors have been placed at the cavity to measure the temperature increase due to rf power. Up to 300 W cw has been coupled to the cavity. Sensor 1 is located at the end-cell region, sensor 2 and sensor 3 close to the stem base, and sensor 4 is located at the outer tank wall. The higher the current density, the higher is the obtained temperature.

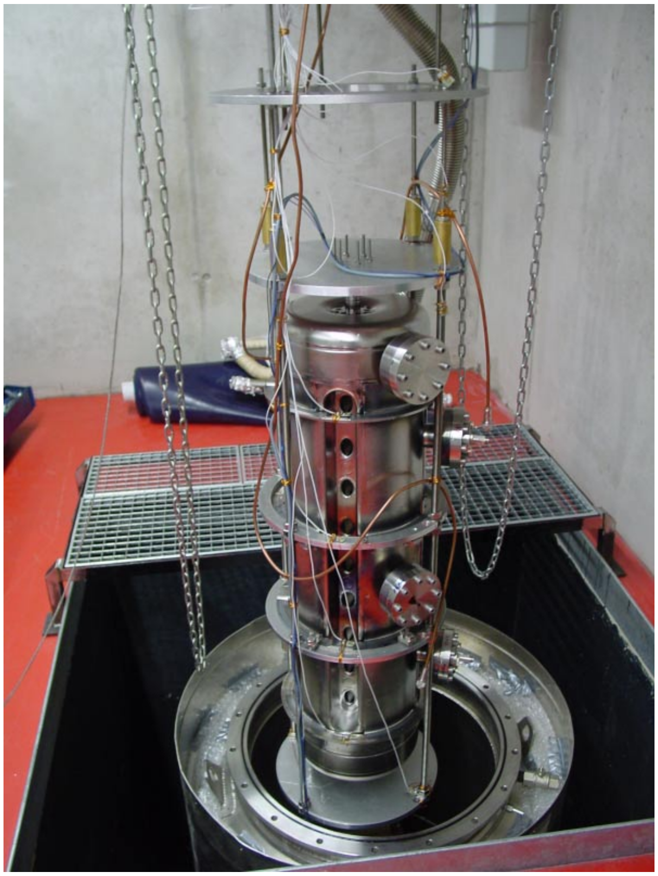

FIG. 27. (Color) Experimental setup for the first cryotest of the CH prototype.

simplifies multipacting conditioning. The coupling factor of the input coupler β_e,

$$\beta_e = \frac{Q_0}{Q_e} = \frac{P_e}{P_c}, \tag{4}$$

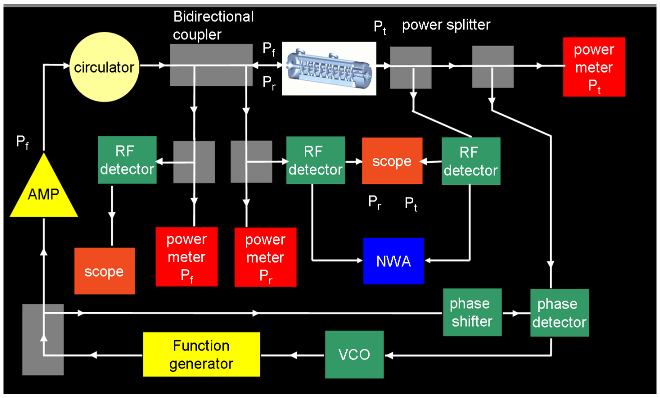

FIG. 28. (Color) Principle of the rf control system to operate the cavity in a closed loop.

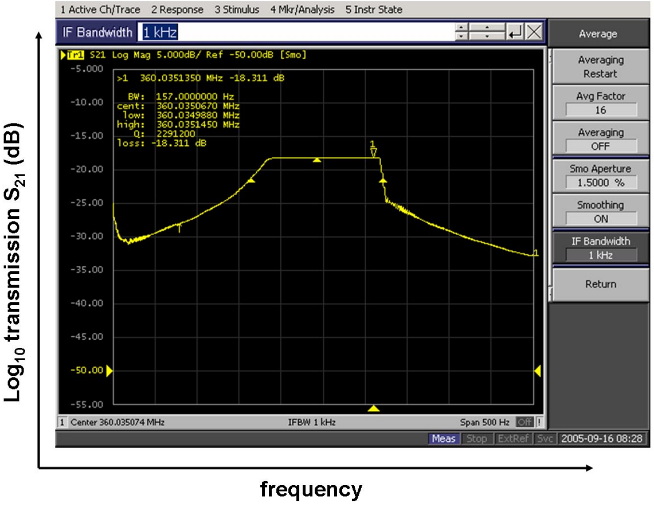

```
Tr1 S21 Log Mag 5.000dB/ Ref -50.00dB [Smo]
>1  360.0351350 MHz -18.311 dB
  BW:  157.0000000 Hz
cent:  360.0350670 MHz
 low:  360.0349880 MHz
high:  360.0351450 MHz
   Q:  2291200
loss: -18.311 dB
1 Center 360.035074 MHz          IFBW 1 kHz          Span 500 Hz
```

FIG. 29. (Color) Measurement of the transmission (S_{21} parameter) as a function of the frequency. The frequency bandwidth is 500 Hz and the y scale is 10 dB/division. At low field levels (forwarded power ≈ mW). the cavity showed multipacting as it can be recognized by the flattop of the resonance curve.

has been measured with different methods (pulsed mode and cw). β has been determined to 4. The unloaded or intrinsic Q-value Q_0 of the CH-prototype cavity is then 5.7×10^8. With a geometrical factor G [38],

$$G = Q_0 R_s = 56\ \Omega, \tag{5}$$

the total surface resistance

$$R_s = R_{\text{BCS}} + R_{\text{mag}} + R_{\text{res}} \tag{6}$$

results to 96 nΩ. The BCS surface resistance for niobium can be calculated with [38]

$$R_s(\text{BCS}) = 2 \times 10^{-4} \frac{1}{T} \left(\frac{f}{1.5}\right)^2 \exp\left(-\frac{17.67}{T}\right)\ \Omega. \tag{7}$$

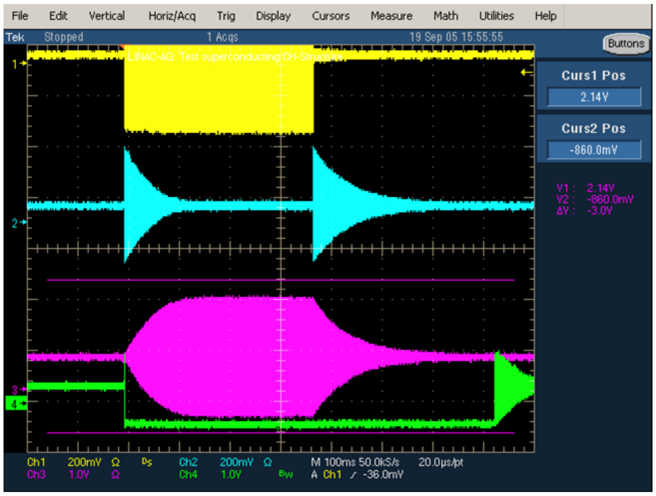

```
Tek   Stopped          1 Acqs          19 Sep 05 15:55:55
LINAC-AG: Test superconducting CH-Structure
V1 :  2.14V
V2 :  -860.0mV
ΔV :  -3.0V
Ch1   200mV  Ω   Ds   Ch2   200mV  Ω        M 100ms 50.0kS/s    20.0µs/pt
Ch3   1.0V   Ω        Ch4   1.0V       Bw   A  Ch1  ⟋  -36.0mV
```

FIG. 30. (Color) The rf signals of the CH cavity at high fields: Reflected signal (green), transmitted (pickup) signal (magenta), and forwarded signal (yellow). The time scale is 100 ms per division.

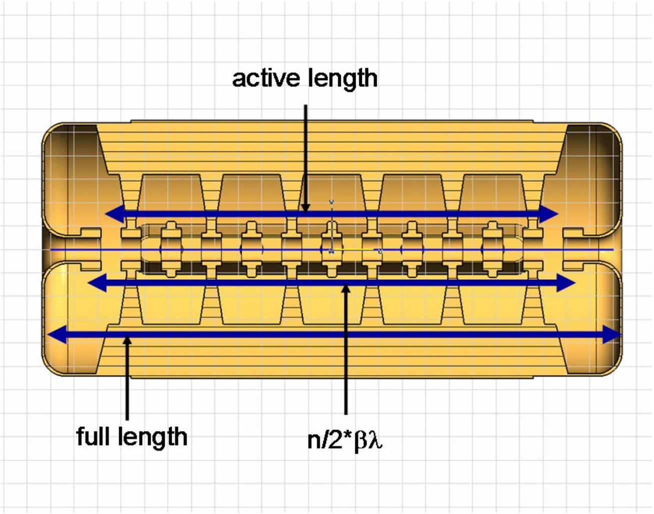

FIG. 31. (Color) Commonly used length definitions in a cavity and their illustration with respect to CH cavities.

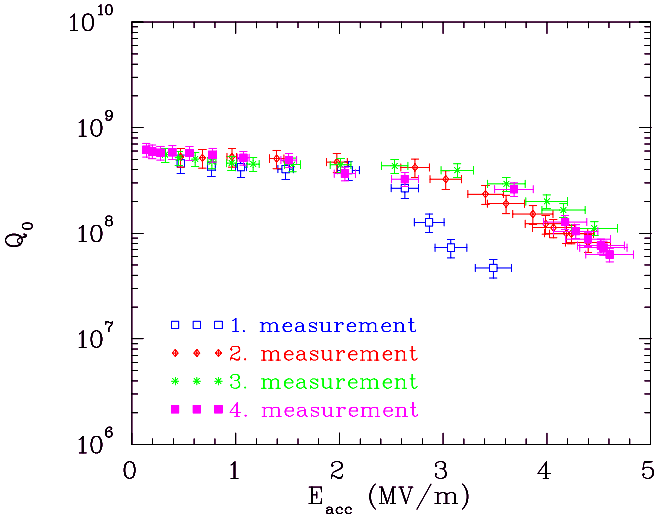

FIG. 32. (Color) The intrinsic Q-value as a function of the effective accelerating gradient based on the $\beta\lambda$ definition.

The frequency of 0.36 GHz and a temperature of 4.45 K give a R_s(BCS) of 49 nΩ. The external magnetic field leads to additional losses due to trapped magnetic flux [38]:

$$R_{\mathrm{mag}} = 0.3[\mathrm{n}\Omega]H_{\mathrm{ext}}[\mathrm{mG}]\sqrt{f[\mathrm{GHz}]}\,[\mathrm{n}\Omega]. \qquad (8)$$

The residual magnetic field of 2 μT increases R_s by 4 nΩ, additionally. The residual resistance R_{res} from (6) is then 43 nΩ for this cavity. The most important measurement was the intrinsic Q-value Q_0 as a function of the accelerating gradient E_a. Unfortunately there are different definitions of the accelerating gradient depending on the defined length in the cavity. The three most common definitions are based on the active length (iris-iris), the $\beta\lambda$ length, and the total cavity length. The $\beta\lambda$ length represents the length in which the electric field on axis is present. In case of the $\beta\lambda$ definition, the considered length in an n-gap structure is $(n/2)\beta\lambda$. Figure 31 shows the different length definitions in the CH structure. Table II summarizes the achieved gradients depending on the different length definitions in use. The gradient which has been achieved based on the $\beta\lambda$ definition is 4.6 MV/m. Figure 32 shows the Q_0 over the E_a curve for the $\beta\lambda$ definition and Fig. 33 shows the intrinsic Q-value as a function of the effective accelerating voltage. The highest voltage which has been achieved is 3.73 MV. The gap voltage amplitudes vary from 200 to 270 kV (Fig. 34). The achieved maximum voltage corresponds to an electric peak field of 25 MV/m and to a magnetic peak field of 26 mT. At peak fields above 20 MV/m, x rays from field emission could be observed. Presently field emission is the limitation of the prototype cavity. The power $P_c = P_f - Pr - P_t$ dissipated in the cavity at the highest field level was 43 W measured with power meters. Additionally, the power has been determined calorimetrically by measuring the amount of evaporating helium. This measurement gave a power of 40 W which is in good agreement with the above-mentioned value. The static losses of the cryostat are in the order of 1 W. The sensitivity of the resonance frequency against external pressure variations has been measured by varying the pressure in the cryostat between 0.3 and 1 bar. Figure 35 shows a linear dependence of the frequency from

TABLE II. Different length and gradient definitions in the CH cavity.

	L = active	$L = 9.5\beta\lambda$	L = total
L (mm)	767	810	1048
E_a (MV/m)	4.86	4.60	3.56
U_a (MV)	3.73	3.73	3.73

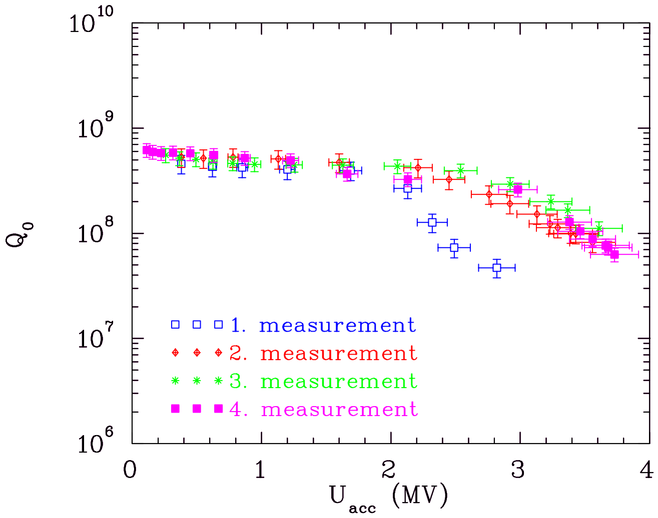

FIG. 33. (Color) The intrinsic Q-value as a function of the effective accelerating voltage. The highest voltage which has been achieved is 3.8 MV.

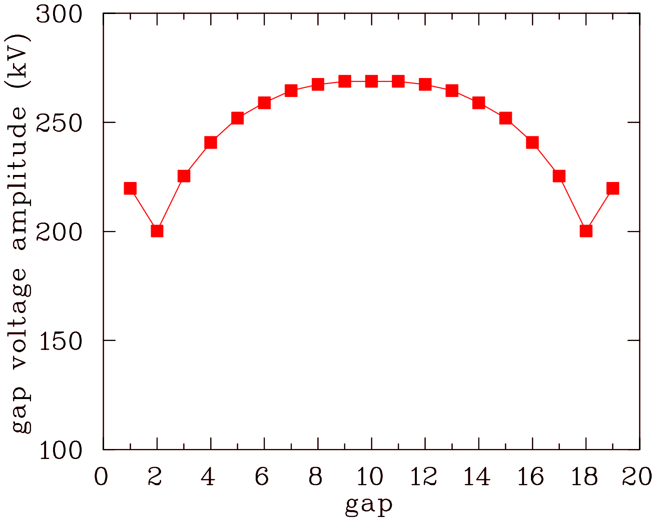

FIG. 34. (Color) Maximum gap voltage amplitudes as achieved during the test runs.

the pressure. The sensitivity df/dp is 250 Hz/mbar. This measurement has been performed at a temperature of 77 K. Then the Lorentz force detuning (LFD) has been measured. This frequency shift is caused by the pressure of the electromagnetic field on the cavity walls. The static detuning is given by [39]

$$\Delta f = -KE_a^2,$$

where K is the LFD constant. The measured K value is 8 Hz/(MV/m)^2 (see Fig. 36). Assuming an accelerating gradient of 3.9 MV/m ($\lambda\beta$ definition), this results in a frequency shift of 120 Hz. The relatively high value of the Lorentz force detuning is mainly caused by using only 2 mm thick niobium sheets. Above peak field levels of 20 MV/m strong field emission has been observed. Several x-ray thermoluminescence dosimeter (TLD) detectors have been placed along the cavity to measure the dose. Figure 37 shows the measured dose along the cavity. The measurement shows a very strong radiation level close to the cavity center which indicates a single field emitter.

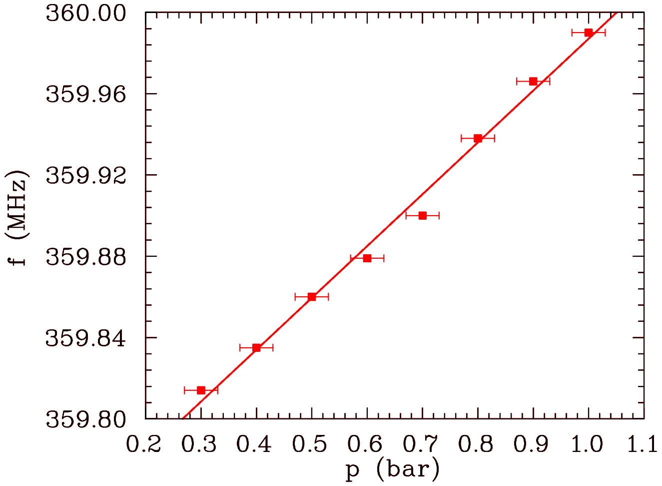

FIG. 35. (Color) Measured sensitivity of the resonance frequency against external pressure variations.

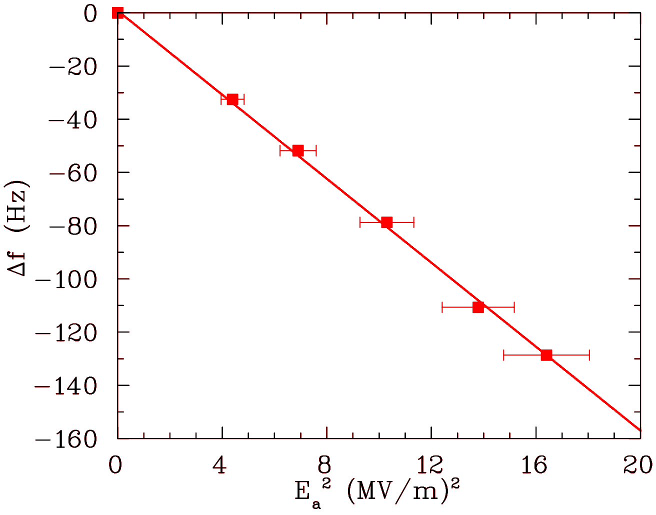

FIG. 36. (Color) Measured frequency shift due to Lorentz force detuning (gradient based on $\beta\lambda$ definition).

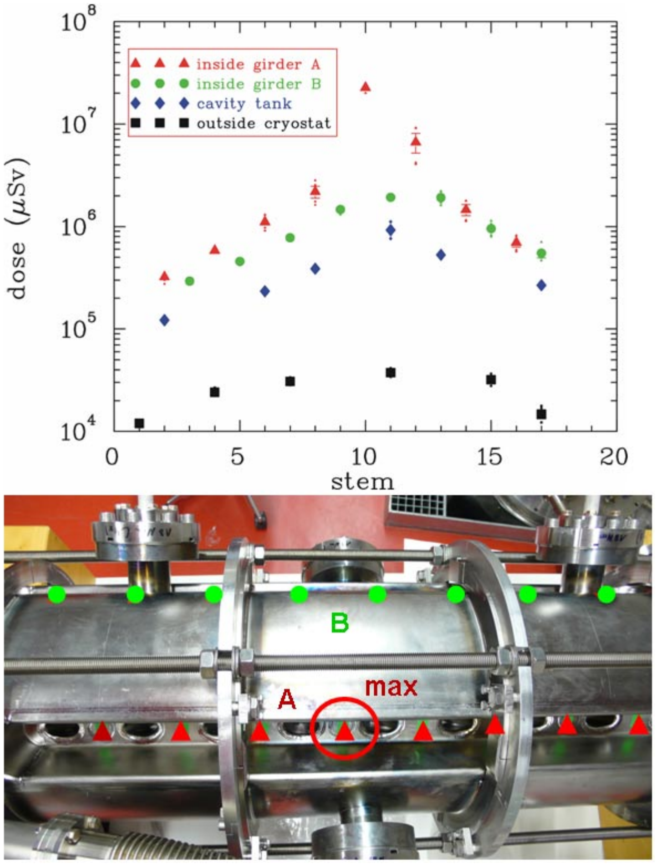

FIG. 37. (Color) Measured x-ray dose along the CH structure (top) and position of the x-ray TLD detectors inside the girders.

XI. MECHANICAL ANALYSIS

The mechanical analysis of the CH structure refers to the cavity deformation under mechanical and thermal loads at liquid helium temperatures. Mechanical loads are either applied on the surface like the hydrostatic vacuum pressure on the cavity surface or are initiated by controlled external forces. Every deformation results in a change of the rf eigenfrequency and might potentially be used to tune the cavity. All loads have to be limited by fracture criteria to avoid a mechanical damage of the structure. The first experimental evidence of a frequency shift is observed by cooldown of the structure which results in a homogeneous contraction. If the cavity is unconstrained no additional stresses occur in the material. The measured changes in frequency can be compared with calculated values, obtained by uniformly scaling the model for the MWS analysis according to temperature dependent contraction data for niobium [40]. Figure 38 shows the comparison, where the red data points are related to the experiments and the blue data points show the simulation results. With respect to cavity tuning, the effect of an external force applied on the outer half drift tubes along the beam axis has been analyzed. Since the body of the structure is quite rigid only the deformation of the end walls is considered. The finite element method tools that have been used to solve the structural mechanical problem are COMSOL multiphysics [41] and ANSYS [42]. The result of the simulation at an applied force of 4 kN is represented by the distribution of the von Mises stress σ_v that is defined by

$$\sigma_v := \sqrt{\frac{(\sigma_1 - \sigma_2)^2 + (\sigma_2 - \sigma_3)^2 + (\sigma_3 - \sigma_1)^2}{2}}, \qquad (9)$$

where $\sigma_1, \sigma_2, \sigma_3$ are the principal stresses. Figure 39 shows the deformed end caps from the inner side of the cavity. The red shaded regions depict the maximum values for the von Mises stress. The maximum van Mises stresses in dependence from the externally applied longitudinal force are plotted in Fig. 40. Negative external forces means pulling on both ends of the structure. The minimum of the van Mises stress is not reached at zero external force, because it is assumed that the cavity is under vacuum and the atmospheric pressure applies on the outer surface. In order to calculate the shift in rf frequency, the undeformed end walls in the model for the MWS simulation have been replaced by the deformed ones for several values of the external forces while using the same mesh. The main rf relevant effect is the change in capacitance due to a variation of the end gap lengths. The result of this analysis is presented in Fig. 41. Exactly this effect will be used for resonant rf tuning of the cavity during operation. As only

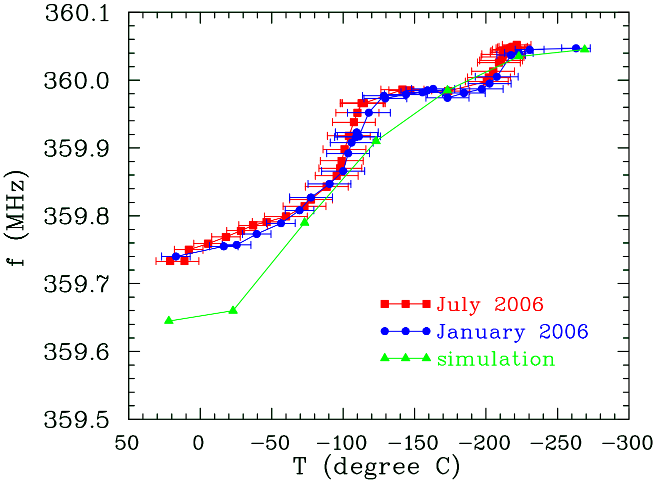

FIG. 38. (Color) Measured (red, blue) and simulated frequency shift during the cooldown. The frequency shift during different cooldowns was very reproducible.

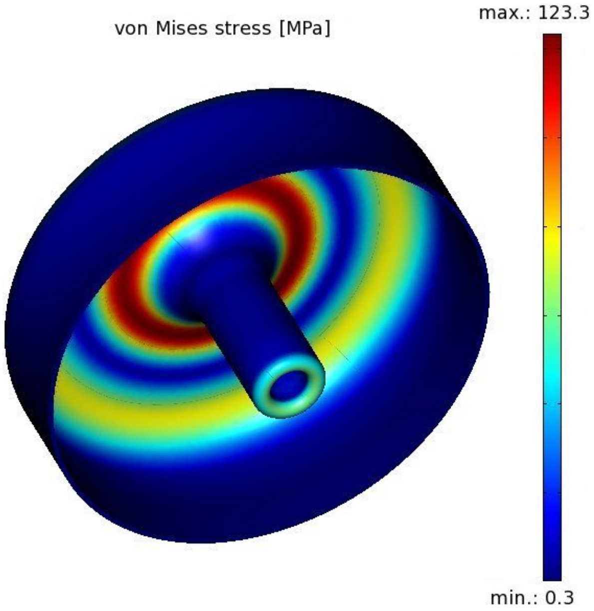

FIG. 39. (Color) The stress load distribution on the deformed end caps with an applied external force of 4 kN.

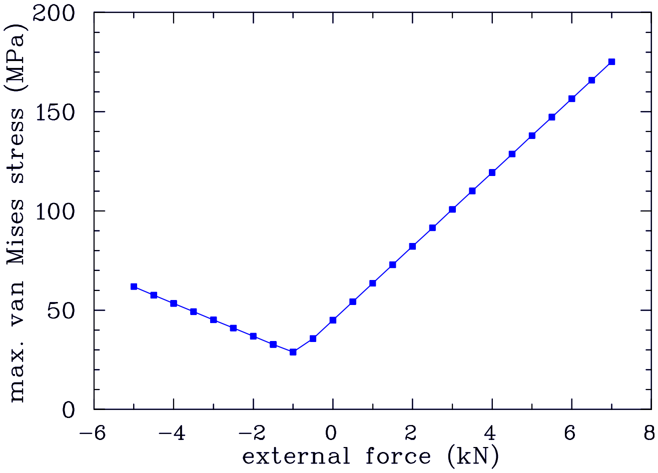

FIG. 40. (Color) Maximum values for the van Mises stress.

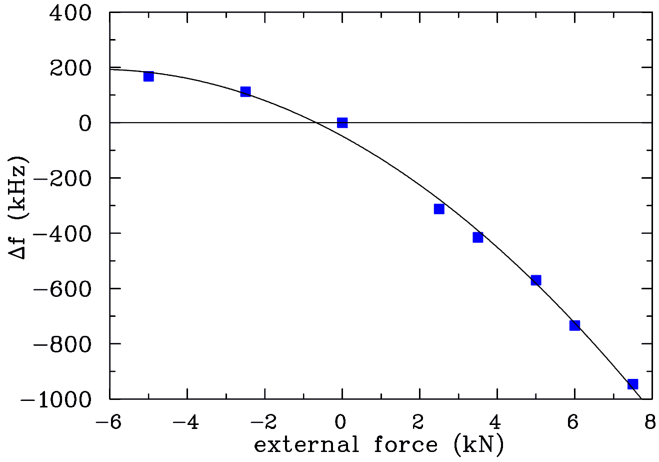

FIG. 41. (Color) Shift in rf frequency due to an external force.

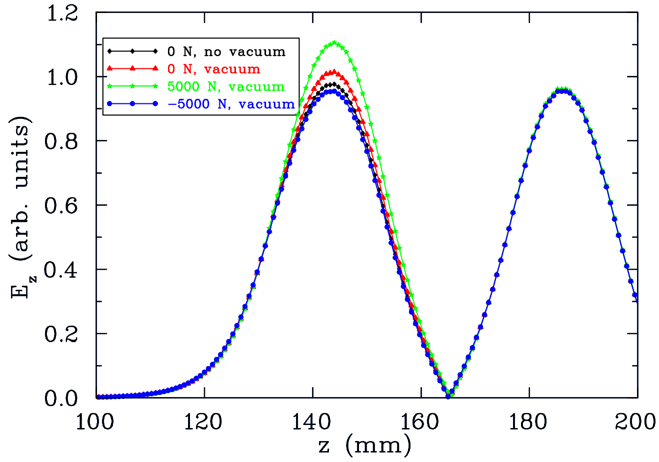

FIG. 42. (Color) Simulated influence of the external vacuum pressure and of the external force of the tuner on the electric field distribution.

the end gaps are affected by that tuning concept, the influence on the gap voltage distribution for each individual cavity layout will limit the applicable tuning range. The mechanical tuning mechanism and the integration into a cryostat can then be quite similar as developed already to a high standard within the TESLA collaboration coordinated by DESY, Hamburg. Figure 42 shows the influence of the external tuning force and the vacuum pressure on the electric field distribution. Applying a positive force (pushing), the first and the last gap become smaller and the field is increased. The curves are normalized to the electric field obtained without vacuum pressure and without an external force.

XII. COMPARISON: THE CH STRUCTURE VS OTHER SC CAVITIES

The development of superconducting low and intermediate-energy cavities is presently a very vital research area. As a result, there is a rapidly growing number of different cavities which are being developed or tested. To assess the properties of the superconducting CH structure, several geometrical and radio frequency parameters have been compared with other cavities which have been built or which are under construction [6,7,9,10,12,36,43–53]. Figure 43 shows the number of accelerating cells per cavity as a function of β. The shaded area is the typical regime for superconducting CH structures as considered for the IFMIF and the EUROTRANS project. This figure makes clear that the CH structure is the first real superconducting multigap structure for the low and intermediate-energy regime. Because of a wide spread of measured surface resistances of individual cavities which depends on temperature, magnetic shielding, material properties, and surface preparation, it is advantageous to compare rf figures of merit which are only determined by the geometry and not by the resistance. The quantities G, R_a/Q_0, and $G(R_a/Q_0) = R_aR_s$ are adequate in that case. Table III summarizes the rf parameters which have been used to compare the CH cavity with other superconducting cavities. Figure 44 shows the geometrical factor G as a function of β. G is defined by

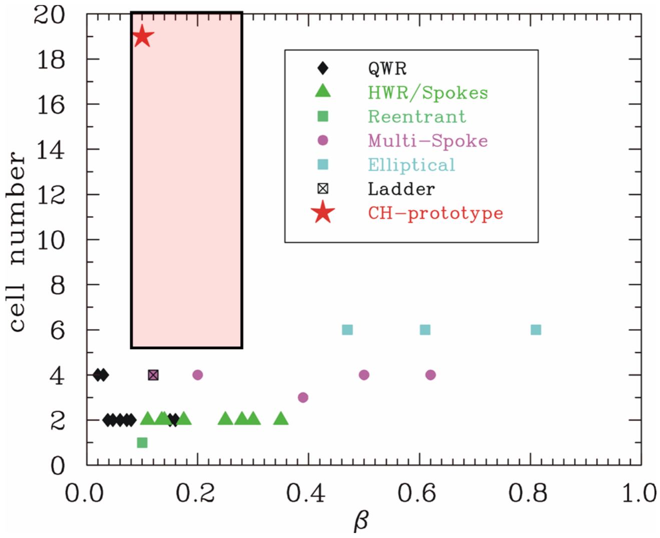

FIG. 43. (Color) Number of accelerating cells per cavity as a function of β.

$$G = R_sQ_0 = \frac{\omega_0\mu_0 \int_V |\mathbf{H}|^2 dV}{\int_S |\mathbf{H}|^2 ds}\ [\Omega].$$

TABLE III. Most important rf parameters of superconducting cavities.

Parameter	Unit	Meaning
E_p/E_a	$\cdots$	Field emission
B_p/E_a	mT/(MV/m)	Thermal breakdown
$G = R_sQ_0$	Ω	Geometrical Q-value
R_a/Q_0	Ω	Geometrical impedance
R_aR_s	Ω^2	Cryogenic load

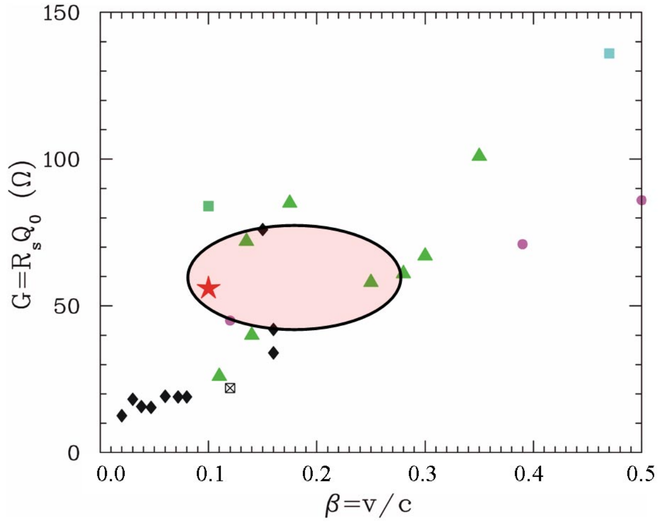

FIG. 44. (Color) Geometrical factor $G = R_sQ_0$ as a function of β. See the legend in Fig. 43.

G is independent of the surface resistance and measures the unloaded Q-value for a given resistance. Typical values of G are some 10 Ω. The geometrical factor of CH structures is comparable with half-wave or spoke cavities with the same β. The geometrical impedance R_a/Q_0 value is defined by

$$\frac{R_a}{Q_0} = \frac{(\int E_z \cos(\frac{\omega_0 z}{\beta c})dz)^2}{\frac{1}{2}\omega_0\epsilon_0 \int_V |\mathbf{E}|^2 dV} \; [\Omega].$$

The ratio between the square of the accelerating voltage and the stored electric field energy measures the capability of the cavity to concentrate the electric field on axis. Figure 45 shows the R_a/Q_0 value as a function of β. The geometrical impedance of CH structures is very high because of the large number of cells and because of the pronounced E-field concentration around the beam axis. For a given length R_a/Q_0 is inversely proportional to β.

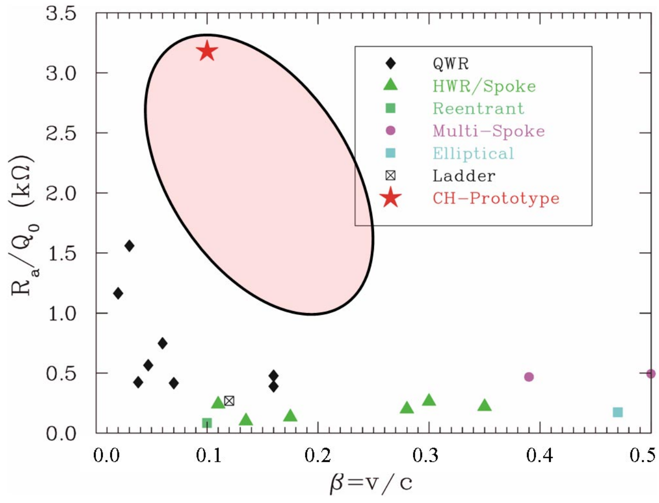

FIG. 45. (Color) R_a/Q_0 value as a function of β.

Another important figure of merit is the value of $G(R_a/Q_0) = R_sR_a$. The power P dissipated in a cavity is given by

$$P = \frac{U_a^2}{R_a} = \frac{U_a^2}{(\frac{R_a}{Q_0})G}R_s = \frac{U_a^2}{(R_aR_s)}R_s.$$

R_aR_s is independent of the surface resistance and depends only on the geometry of the cavity. It measures the cryogenic load and is therefore especially important for cw operated accelerators. R_aR_s is directly proportional to the length of the cavity and the number of cells, respectively. To compare different cavity types, Fig. 46 shows the R_aR_s value per cell as a function of β. Typical values are several $k\Omega^2$. The average R_aR_s value of CH structures is about twice as high as for half-wave resonators with the same β. This means that for the same cryogenic heat load the surface resistance of the CH structure can be higher by a factor of 2. The peak field ratios E_p/E_a and B_p/E_a are significant especially for superconducting cavities. High electric peak field can lead to field emission with its typical Q drop whereas the magnetic field typically can trigger a thermal breakdown of superconductivity. For a good cavity performance the peak fields should be kept as low as possible. Figures 47 and 48 show the ratios E_p/E_a and B_p/E_a, respectively. In both cases the $\beta\lambda$ definition of the gradient has been used. It shows that CH structures have electric peak fields which are comparable with quarter-wave and half-wave resonators. Because of the complex geometry and the difficult surface preparation, it is likely that CH structures will be mostly limited by field emission. This is confirmed by our first experience with the CH-prototype cavity. The magnetic peak field in CH structures is very low compared with quarter-wave and half-wave resonators. The reason is the quite homogeneous distribution of losses due to the H mode. CH structures and multi-

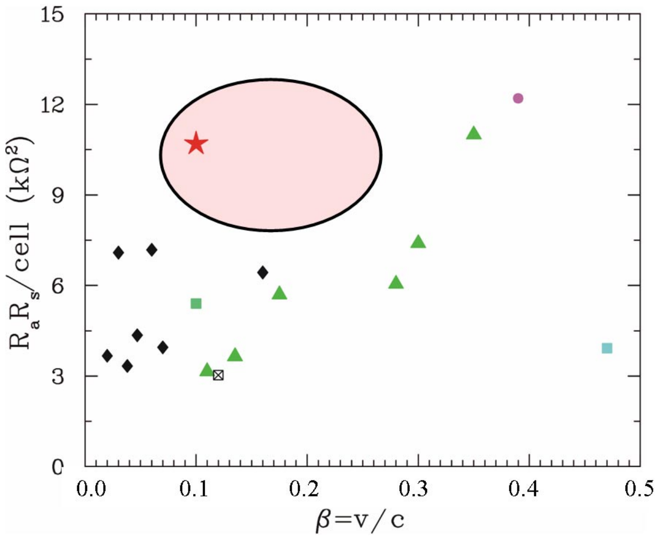

FIG. 46. (Color) R_aR_s per cell as a function of β. See the legend in Fig. 45.

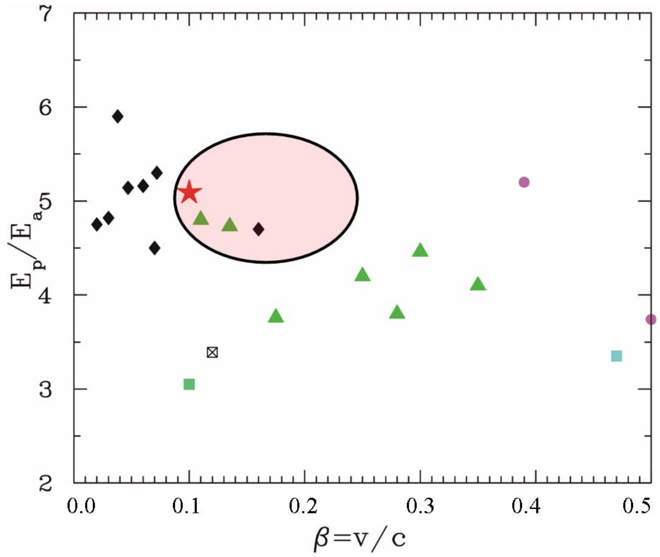

FIG. 47. (Color) Ratio E_p/E_a of the electric peak field and accelerating field as a function of β. The values are based on the $\beta\lambda$ definition. See the legend in Fig. 45.

spoke cavities have some common properties resulting from the cross-bar geometry and the used H mode. Main differences are the "drift tube in stem concept" of the CH structure as well as the girders: These provide an efficient way for strong capacitive rf coupling and for tuning the resonance frequency as well as the gap voltage distribution. It was technically quite easy to establish the zero mode for CH structures with an end-cell geometry described above. With these achievements the CH structure is ready for use as a multicell cavity with graded β profile. Negative synchronous particle structures as well as KONUS-type structures may exploit this potential in future designs.

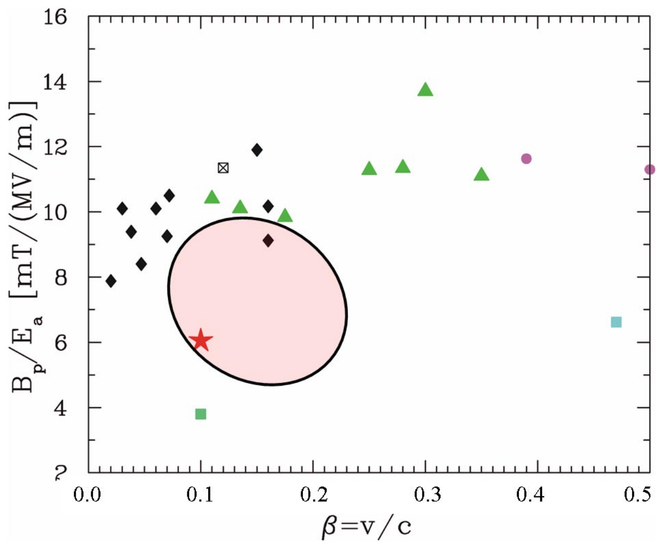

FIG. 48. (Color) Ratio B_p/E_a of the magnetic peak field and accelerating field as a function of β. The values are based on the $\beta\lambda$ definition. See the legend in Fig. 45.

XIII. SUMMARY AND OUTLOOK

The CH structure operated in the H_{21}-mode is a novel multicell drift-tube cavity which can be realized for room temperature as well as for superconducting operation. Different tuning and rf coupling methods have been studied using a room temperature CH model. In general, the agreement between simulations and measurements have been excellent. A superconducting 19-cell $\beta = 0.1$ prototype cavity has been developed and built. First cold tests of the CH cavity have been performed successfully in the new cryogenic rf laboratory in Frankfurt. An effective accelerating voltage of 3.7 MV has been achieved. It is planned to treat the cavity surface again with buffered chemical polishing and high pressure rinsing to reduce the observed field emission which caused the pronounced x-ray radiation from one cell at present. Additionally, the development of a tuner system (slow and fast) and preparations for cavity operation in a horizontal cryostat have been started. The superconducting CH structure is well suited for the low and medium energy range of proton and ion driver linacs. There are several projects under consideration (cw linac for super heavy element production, EUROTRANS, IFMIF) which could profit from the advantages of the CH structure [4,54–56].

ACKNOWLEDGMENTS

This work has been supported by Gesellschaft für Schwerionenforschung (GSI), BMBF Contract No. 06F134I, and EU Contract No. 516520-FI6W. We acknowledge also the support of the European Community-Research Infrastructure Activity under the FP6 "Structuring the European Research Area" program (CARE, Contract No. RII3-CT-2003-506395) and EU Contract No. EFDA/99-507ERB5005 CT990061 between EURATOM/FZ Karlsruhe IAP-FU. The work was carried out within the framework of the European Fusion Development Agreement. The views and opinions expressed herein do not necessarily reflect those of the European Commission. The authors would like to thank the company ACCEL for the excellent work on technical drawings as well as in the fabrication of the prototype cavity. In addition, the authors would like to thank the technical staff of the IAP in Frankfurt, especially D. Bänsch, I. Müller, G. Hausen, and S. Reploeg. They would also like to thank H. Deitinghoff for the administrative project work and K. Dermati, GSI Darmstadt, for the support with mechanical simulations.

---

[1] K. W. Shepard, in Proceedings of the 2002 Linear Accelerator Conference, Gyeongju, South Korea, pp. 596–599.

[2] T. Junquera *et al.*, in Proceedings of the 2004 European Particle Accelerator Conference, Lucerne, Switzerland, pp. 1285–1287.

[3] J.-L. Biarotte, in Proceedings of the 2004 Linear Accelerator Conference, Lübeck, Germany, pp. 275–279.

[4] Technical Report, IFMIF International Team, IFMIF Comprehensive Design Report, International Energy Agency, 2004.

[5] A. Pisent *et al.*, in Proceedings of the 2004 European Particle Accelerator Conference, Lucerne, Switzerland, pp. 857–859.

[6] A. Facco *et al.*, in Proceedings of the 2004 European Particle Accelerator Conference, Lucerne, Switzerland, pp. 1012–1014.

[7] T. Tajima *et al.*, in Proceedings of the 2002 Linear Accelerator Conference, Gyeongju, South Korea, pp. 228–230.

[8] R. Stassen *et al.*, in Proceedings of the 2004 Linear Accelerator Conference, Lübeck, Germany, pp. 821–823.

[9] J. Fuerst *et al.*, in Proceedings of the 2003 Particle Accelerator Conference, Portland, OR, USA, pp. 1294–1296.

[10] T. L. Grimm *et al.*, in Proceedings of the 2003 Particle Accelerator Conference, Portland, OR, USA, pp. 1353–1355.

[11] M. P. Kelly *et al.*, in Proceedings of the 2004 Linear Accelerator Conference, Lübeck, Germany, pp. 608–611.

[12] K. Shepard *et al.*, in Proceedings of the 2005 Particle Accelerator Conference, Knoxville, TN, USA, pp. 4344–4346.

[13] U. Ratzinger, Habilitationsschrift, Universität Frankfurt, Germany, 1999.

[14] U. Ratzinger and R. Tiede, Nucl. Instrum. Methods Phys. Res., Sect. A **415**, 229 (1998).

[15] H. Podlech, in Proceedings of the 2004 Linear Accelerator Conference, Lübeck, Germany, pp. 28–32.

[16] G. Amendola *et al.*, in Proceedings of the 1992 European Particle Accelerator Conference, pp. 536–538.

[17] U. Ratzinger *et al.*, in Proceedings of the 1987 Particle Accelerator Conference, pp. 367–368.

[18] U. Ratzinger, in Proceedings of the 2000 European Particle Accelerator Conference, Vienna, Austria, pp. 98–102.

[19] J. D. Schneider, in Proceedings of the 2000 European Particle Accelerator Conference, Vienna, Austria, pp. 118–122.

[20] N. Angert *et al.*, in Proceedings of the 1992 European Accelerator Conference, pp. 167–169.

[21] Y. R. Lu *et al.*, in Proceedings of the 2004 Linear Accelerator Conference, Lübeck, Germany, pp. 57–59.

[22] S. Emhofer *et al.*, in Proceedings of the 2000 European Accelerator Conference, pp. 809–811.

[23] J. Broere *et al.*, in Proceedings of the 1998 Linear Accelerator Conference, Argonne, IL, USA, pp. 771–773.

[24] E. Nolte *et al.*, Nucl. Instrum. Methods **158**, 311 (1979).

[25] R. Laxdal *et al.*, in Proceedings of the 2001 Particle Accelerator Conference, Chicago, IL, USA, pp. 3942–3944.

[26] U. Ratzinger, in Proceedings of the 1991 Particle Accelerator Conference, pp. 567–571.

[27] U. Ratzinger, Nucl. Instrum. Methods Phys. Res., Sect. A **464**, 636 (2001).

[28] R. Eichhorn *et al.*, in Proceedings of the 2002 Linear Accelerator Conference, Gyeongju, South Korea, pp. 479–481.

[29] H. Liebermann, Ph.D. thesis, Universität Frankfurt, Germany, 2006.

[30] http://www.cst.com.

[31] H. Podlech *et al.*, in Proceedings of the 2003 Superconducting RF Workshop, Travemünde, Germany.

[32] M. Stirbet *et al.*, in Proceedings of the 2001 Particle Accelerator Conference, Chicago, IL, USA, pp. 1125–1127.

[33] E. Kako *et al.*, in Proceedings of the 2003 Particle Accelerator Conference, Portland, OR, USA, pp. 1338–1340.

[34] H. Sakai *et al.*, in Proceedings of the 2005 Particle Accelerator Conference, Knoxville, TN, USA, pp. 1294–1296.

[35] P. Balleyguier, in Proceedings of the 1998 Linear Accelerator Conference, Argonne, IL, USA, pp. 133–135.

[36] R. Stassen, Ph.D. thesis, Universität Frankfurt, Germany, 2005.

[37] http://www.accel.de.

[38] H. Padamsee, J. Knobloch, and T. Hays, *RF Superconductivity for Accelerators* (Wiley, New York, 1998).

[39] A. Mosnier, Technical Report TESLA 93-09, DESY, 1993.

[40] *Handbook on Materials for Superconducting Machinery* (Metals and Ceramics Information Center, Columbus, OH, 1977).

[41] http://www.comsol.com.

[42] http://www.ansys.com.

[43] G. Olry *et al.*, in Proceedings of the 2004 European Particle Accelerator Conference, Lucerne, Switzerland, pp. 1003–1005.

[44] A. Müller *et al.*, WP-DEL/03/048, 2004.

[45] K. Shepard and T. Tretyakova, in Proceedings of the 2000 Linear Accelerator Conference, Monterey, CA, USA, pp. 920–922.

[46] A. Facco *et al.*, in Proceedings of the 2004 European Particle Accelerator Conference, Lucerne, Switzerland, pp. 1015–1017.

[47] C. Compton *et al.*, Phys. Rev. ST Accel. Beams **8**, 042003 (2005).

[48] V. Andreev *et al.*, Phys. Rev. ST Accel. Beams **6**, 040101 (2003).

[49] P. Ostroumov *et al.*, in Proceedings of the 2005 Particle Accelerator Conference, Knoxville, TN, USA, pp. 3360–3362.

[50] M. Comunian *et al.*, in Proceedings of the 2002 European Particle Accelerator Conference, Paris, France, pp. 64–66.

[51] A. Facco *et al.*, in Proceedings of the 2001 Particle Accelerator Conference, Chicago, IL, USA, pp. 1092–1094.

[52] T. Grimm *et al.*, in Proceedings of the 2003 Superconducting RF Workshop, Travemünde, Germany.

[53] K. Shepard, in Proceedings of the 2003 Particle Accelerator Conference, Portland, OR, USA, pp. 581–

585.
[54] U. Ratzinger, Nucl. Phys. **A701**, 641 (2002).
[55] R. Eichhorn, in Proceedings of the 2001 Accelerator Conference, Chicago, IL, USA, pp. 495–499.
[56] T. Junquera, in Proceedings of the of the International Workshop on P&T and ADS Development, Mol, Belgium.
[57] G. Clemente *et al.*, in Proceedings of the 2006 European Particle Accelerator Conference, Edinburgh, UK, pp. 1283–1285.